Time-dependent density functional study of transport in molecular junctions

Kálmán Varga

Phys. Rev. B **83**, 195130 — Published 25 May 2011

DOI: 10.1103/PhysRevB.83.195130

Time-dependent density functional study of transport in molecular junctions

Kálmán Varga
Department of Physics and Astronomy, Vanderbilt University, Nashville, TN 37235

Electron transport in nanostructures is calculated and compared using a time-independent and a time-dependent first-principles framework. The time-independent approach uses the non-equilibrium Green's function technique to calculate the current, while the time-dependent method extracts the current from the time propagated wave function. The approaches have been tested using gold-benzene-dithiolate-gold and gold-bipyridine-gold molecular junctions. The reasons for the differences in the current-voltage curves predicted by the two methods are discussed.

I. I. INTRODUCTION

The non-equilibrium Green's function approach (NEGF)[1–3], combined with the density functional theory (DFT)[4] Hamiltonian is one of the most important tools to describe steady state electron transport in nanostructures. DFT provides a single particle framework with an effective Hamiltonian. Powerful approaches have been developed for localized basis representations of the DFT Hamiltonian[5]. The localized basis representation facilitates a straightforward and efficient implementation of NEGF using simple matrix algebra. Due to the simplicity of the formulation the NEGF-DFT framework, it has become a popular approach to calculate transport properties of nanostructures[2,6–15]. This approach is based on the assumption that ground state DFT provides a good approximation to the current-carrying scattering states in a non-equilibrium transport process. The calculated transport properties, however, do not fully agree with the experiments; the calculated conductances, for example, are typically an order of magnitude larger[16] than the experimentally observed ones. This discrepancy, together with the fact that there are emerging experiments measuring time-dependent transport properties[17,18] motivated the application of time-dependent density functional theory (TDDFT)[19] to study the problem of electron transport.

Transport calculation schemes based on TDDFT have been proposed as an alternative to the NEGF-DFT framework[20–35]. Electron transport is an intrinsically dynamical non-equilibrium process, therefore, the time-dependent approach is a more natural choice to solve quantum transport problems. In TDDFT the time-dependent density of an interacting system moving in an external time-dependent local potential can be calculated using a fictitious system of non-interacting electrons in a local, effective time-dependent potential. The TDDFT approach is expected to improve several shortcomings of the NEGF-DFT approach:

(1) In static DFT, the transmission functions are computed at the non-interacting Kohn-Sham excitation energies, which in general do not coincide with the true excitation energies. The true excitation energies of interacting systems are accessible using TDDFT.

(2) The NEGF-DFT approach is based on an unphysical separation of the system into disconnected parts (contacts and device/molecule) at infinite past[20,22]. In the remote past the left and right electrodes are disconnected and are in equilibrium with two different chemical potentials; the conducting part of the Hamiltonian is switched on adiabatically and eventually a steady state develops. This artificial partitioning introduces subtle questions about how the steady state is reached[25]. TDDFT can be used in a partition-free framework[21] allowing the inclusion of interaction between the electrodes and the device in a realistic way.

A number of theoretical works have been devoted to laying down the foundation of transport calculations in the framework of TDDFT[20,36–39]. Stefanucci and Almbladh[20] have derived exact equations of motion for the two-time Green's functions using TDDFT. This approach has been extended to a scheme in which the wave function is propagated in time with open boundary conditions[22]. Alternatively, a microcanonical TDDFT approach has been proposed for finite isolated systems[25] which treats electronic transport as a discharge across a nanocontact connecting two large but finite charged electrodes.

Before the TDDFT calculation of electron transport can become a practical alternative to the static NEGF-DFT approach, a number of technical problems have to be addressed. The present implementations of TDDFT transport calculations fall into two categories. The first approach uses the Green's function formalism in the time domain[23,24,26,40], and the second one is based on the time propagation of the wave function[28,29,31,35,41]. The time domain calculation of the Green's function is not a simple task and the application of the Green's function method is mostly limited to non-self consistent tight binding models. Only a very few self consistent TDDFT calculations have been carried out in the time domain Green's function framework[24].

The second approach, the TDDFT calculation of electron transport by time propagation of the wave function is an attractive alternative because one can exploit the advanced computional methods that have been developed to solve the time-dependent Kohn-Sham equations. Efficient numerical schemes have been proposed and implemented[42–45] to calculate the optical absorption spectrum, nonlinear polarizabilities, dielectric constant, and other physical quantities by direct time propagation of the wave functions. Various time propagators

have been tested[23,44,46] including the Chebyshev, Taylor, and Crank-Nicholson methods. The main challenge in the application of these time propagating approaches in transport calculations is the proper treatment of the boundary conditions. Calculational methods employing absorbing[47] and open[36] boundary conditions have been developed to address this problem.

The aim of this work is to calculate the steady state transport properties in both the time-dependent and time-independent frameworks and compare the calculated conductances and current-voltage characteristics. This question has been raised earlier[20] in the framework of a tight-binding model and the answer was that the dynamical approach quantitatively reproduces the static results.

In this work, we use time-dependent and time-independent first-principles simulation to calculate the electron transport in molecular junctions and compare the calculated current voltage characteristics. To make the two methods comparable, the same simulation cell, Hamiltonian, and basis representation are used in both cases.

TDDFT will be used in the time-dependent approach. It will be shown that by using the domain decomposition method[48,49] to set up an efficient basis and complex absorbing potentials to handle the open boundary conditions, one can calculate the electron current by time propagating the electron orbitals in an external bias.

In the time-independent approach, the transport properties will be calculated using the NEGF method[1–3]. The only significant modification of the standard NEGF method is that the self-energies are calculated with the complex potential approach[50] in the present calculations.

Multidomain decomposition is used to set up the basis and complex absorbing potentials are employed to make the simulation cell finite in both the time-dependent and the time-independent calculations. In the multidomain decomposition approach, one divides the system into smaller overlapping subdomains. The Kohn-Sham equations can be solved independently in each subdomain. Using the subdomain eigenfunctions as basis states one obtains a structured sparse block matrix representation of the Hamiltonian. This structure allows both matrix inversion and matrix multiplication to be performed very efficiently.

The leads are made finite by adding a complex absorbing potential to the leads' Hamiltonian. The complex absorbing potential (CAP) goes to infinity in the asymptotic region, effectively chopping off the lead beyond a certain range. The CAP approach gives the same transmission probability as the NEGF-DFT calculations[50] and allows the propagation of the wave function without reflections from the boundaries.

The outline of the paper is as follows. In Section II the basis functions used in the calculations will be described. Section III will introduce the time-independent approach, and Section IV will show the time-dependent formalism. The results will be presented and discussed in Section V., followed by brief summary in Section VI. To make the paper self-contained the most important expression used in the calculations are collected in an Appendix.

II. II. REPRESENTATION OF THE HAMILTONIAN

In this section we introduce the basis function representation of the Hamiltonian. This representation will be used in the time-propagation of the orbitals in the time-dependent case and in the calculation of the Green's function in the time-independent case. The system consists of a left and a right lead and a central (scattering) region (see Fig. 1). Both the leads and the central region are divided into boxes (domains). The basis representations of these domains are built up from the local solutions of the Kohn-Sham equations. As we have shown in a previous paper[51] these locally optimized basis functions provide an accurate representation for transport calculations.

A. II.1 Domain decomposition

In the domain decomposition approach the system is divided into domains (see Fig. 1). In the present calculations rectangular boxes are used. In the leads the boxes are defined by the periodically repeated supercells. Each domain is described by a basis function set ϕ_j^i where i is the domain index, $(i = 1, \ldots, N)$ and j is the index of the basis function in domain i. The domain basis functions are allowed to overlap with those in the neighboring domains but only with the nearest neighbors. The construction of these basis functions will be discussed in the next subsection. The Hamiltonian and overlap matrices in the ith domain are defined as

$$(H_{Bi})_{kj} = \langle \phi_k^i | H | \phi_j^i \rangle, \qquad (S_{Bi})_{kj} = \langle \phi_k^i | \phi_j^i \rangle, \quad (1)$$

while those in the connecting neighboring domains are

$$(H_{Ai})_{kj} = \langle \phi_k^i | H | \phi_j^{i-1} \rangle, \qquad (S_{Ai})_{kj} = \langle \phi_k^i | \phi_j^{i-1} \rangle. \quad (2)$$

The Hamiltonian and the overlap matrices will be sparse block tridiagonal structured matrices

$$H = \begin{pmatrix} H_{B1} & H_{A2}^\dagger & 0 & 0 & \ldots \\ H_{A2} & H_{B2} & H_{A3}^\dagger & 0 & \ldots \\ & & & & H_{AN}^\dagger \\ 0 & \ldots & & H_{AN} & H_{BN} \end{pmatrix}, \quad (3)$$

$$S = \begin{pmatrix} S_{B1} & S_{A2}^\dagger & 0 & 0 & \ldots \\ S_{A2} & S_{B2} & S_{A3}^\dagger & 0 & \ldots \\ & & & & S_{AN}^\dagger \\ 0 & \ldots & & S_{AN} & S_{BN} \end{pmatrix}, \quad (4)$$

where H_{Bi} (S_{Bi}) are $n_i \times n_i$ and H_{Ai} (S_{Ai}) are $n_i \times n_{i-1}$ matrices. Once the block tridiagonal matrices have been

generated, any linear combination of these matrices, e.g. $F = S + i\frac{\Delta t}{2}H$ which is used in the Crank-Nicholson step, or $F = ES - H$ used in the Green's function calculation, can be factorized by a block-LDL decomposition (see Ref.[48] for details)

$$F = L^\dagger D L = \begin{pmatrix} D_1 & L_1^\dagger & 0 & 0 & \dots \\ L_1 & D_2 & L_2^\dagger & 0 & \dots \\ & & & & L_{N-1}^\dagger \\ 0 & \dots & & L_{N-1} & D_N \end{pmatrix}, \quad (5)$$

where L_i are lower diagonal and D_i are diagonal matrices. Note that the LDL decomposition of a block tridiagonal matrix preserves the block tridiagonal form. The LDL factorization can be generated by a recursive procedure as described in[48]. The advantage of the LDL decomposition is that the inverse of the whole matrix can be easily calculated by forward and backward substitutions using the low dimensional L_i matrices without inverting the entire F matrix directly.

In time-independent transport calculations the Hamiltonian matrix is written in the form[2,3],

$$H = \begin{pmatrix} H_L & H_{LC} & 0 \\ H_{LC}^\dagger & H_C & H_{RC}^\dagger \\ 0 & H_{RC} & H_R \end{pmatrix}, \quad (6)$$

where H_L,H_R and H_C are the Hamiltonian matrices of the left and right leads and of the central region, and H_{LC} and H_{RC} are the coupling Hamiltonians. By comparing Eqs. (3) and (6) one can easily group the domain Hamiltonian matrices of Eq. (3) to set up the matrices in Eq. (6). The details of this mapping are given in Appendix A. Note that the advantage of the domain decomposition is that in addition to H_L and H_R, H_C is also a block tridiagonal matrix and the accuracy of the calculations, as will be shown in the next subsection, can be controlled by the number of basis functions of the domains.

B. II.2 Basis functions

Each domain has its own set of basis functions. The identical domains in the lead region have the same basis function sets. The domain basis functions are defined as the local eigenstates of the domains. The Lagrange basis functions will be used to generate the domain basis functions. Using the Lagrange basis functions the Kohn-Sham equation is solved in each domain. Once a self-consistent potential is obtained, the Kohn-Sham Hamiltonian is diagonalized using the basis functions. The lowest n_i eigensolutions ϕ_j^i are retained in each domain as domain basis functions to represent the Hamiltonian of the whole system.

The Lagrange basis is defined on a grid and each subdomain has its own set of gridpoints. These grids extend beyond the boundary of the domains and so the basis functions in the adjacent domains overlap. In practice a rectangular computational cell is chosen and the computational cell is divided into N intervals in the x direction

$$[a_i, b_i] \quad (i = 1, \dots, N), \quad (7)$$

where $a_{i+1} < b_i$ but $a_i < a_{i+1}$, that is, there is an overlap between the neighboring domains but there is no overlap with the second neighbors (Fig. 2). The overlap, $l_o = b_i - a_{i+1}$ is chosen to be the same for each domain.

The jth basis function in the ith domain is expanded in terms of a tensorial product of Lagrange basis functions[52],

$$\phi_\nu(\mathbf{r}) = \phi_j^i(\mathbf{r}) = \sum_{l=1}^{M_x}\sum_{m=1}^{M_y}\sum_{n=1}^{M_z} C_{j,lmn}^i L_l^i(x) L_m(y) L_n(z), \quad (8)$$

where $\nu = (ij)$. In the x direction, the Lagrange functions are defined on grid points $a_i < x_k^i < b_i$ as

$$L_n^i(x) = \pi_n(x)\sqrt{w(x)}, \qquad \pi_n(x) = \prod_{\substack{k=1 \\ k\neq n}}^{M_x} \frac{x - x_k^i}{x_n^i - x_k^i} \quad (9)$$

where $w(x)$ is the weight function and the index i indicates that the Lagrange function is defined in the ith domain. The computational cell is not divided into domains in the y and z directions. The Lagrange functions $L_m(y)$ and $L_n(z)$ are used in the y and z directions in each domain. These basis functions are defined in the same way as the basis functions in the x direction except that there is no explicit dependence on the domain indices.

Each Lagrange function is nonzero at one grid point and zero at all other grid points, oscillating between the grid points. Due to their continuity and analytical form, these basis functions represent the wave function not only on the grid points but everywhere in space. The Lagrange functions form an orthonormal complete set of states and the convergence of the calculated energy is exponential with respect to basis dimension. On the Lagrange function basis, similar to the finite difference approaches[53–55], the potential energy matrix is diagonal leading to a very sparse Hamiltonian that is ideal for iterative inversion and diagonalization.

There are $M = M_x \times M_y \times M_z$ Lagrange basis functions in each domain. The domain basis functions ϕ_j^k are generated by solving the eigenvalue problem

$$H_{Ak} C_j^k = E_j S_{Ak} C_j^k \quad (10)$$

for C_j^k of eq. (8) and keeping the lowest n_k eigenstates (below a preset cutoff energy, E_{cutoff}).

C. II.3 Complex absorbing potentials

The same finite computational cell will be used in both the time-dependent and time-independent calculations. The finiteness of the computational cell requires proper handling of the wave function at the boundary. This will

be achieved by a complex absorbing potential in both the time-dependent and in the time independent case.

In the conventional time-independent NEGF-DFT transport calculations[2,6–15] the leads are infinite and the Green's functions of the leads have to be calculated for every energy. In the present calculations the leads are made finite by adding a complex absorbing potential to the leads' Hamiltonian. The complex absorbing potential (CAP) goes to infinity in the asymptotical region effectively chopping off the lead beyond a certain range. The CAP approach gives the same transmission probability as the NEGF-DFT calculations[50]. The advantage of the CAP method is that it can be used with a finite computational cell and the computationally demanding calculation of the Green's function of the infinite leads is avoided[50]. Using the CAP the resulted finite dimensional matrices can be diagonalized and the self-energies can be calculated for each energy at once[50].

In the time-dependent calculations the CAP is used to prevent reflections from the boundaries. CAPs are often used in time-dependent quantum mechanical simulations, for example for time-dependent wave packet propagations[56–62]. The complex potentials not only absorb the outgoing waves but can also produce reflections. The construction and optimization of reflection-free CAPs is therefore very important. Many different forms of pure imaginary potential have been investigated, including, power-law[57,59], polynomial[60], and other parameterized functional forms (see[58] for a recent review). Besides purely imaginary potentials, complex potentials have also been proposed[61].

In this work we will adopt the CAP suggested in[62]. This negative, imaginary CAP is derived from a physically motivated differential equation and its form is (see Fig. 3)

$$iw(\mathbf{r}) = -i\frac{\hbar^2}{2m}\left(\frac{2\pi}{\Delta x}\right)^2 f(\tilde{x}) \tag{11}$$

where $\Delta x = x_2 - x_1$, x_1 is the start and x_2 is the end of the absorbing region, c is a numerical constant, m is the electron's mass and

$$f(\tilde{x}) = \frac{4}{c}\left(\frac{1}{(c-\tilde{x})^2} + \frac{1}{(c+\tilde{x})^2} - 2\right), \qquad \tilde{x} = \frac{c(x-x_1)}{\Delta x}. \tag{12}$$

The CAP goes to infinity at the end of the absorbing region and effectively cuts off the leads beyond that distance. The left and right CAPs are $w^L(x)$ and $w^R(x)$ and their starting points, x_1^L and x_1^R are deep inside the lead so the complex potential does not affect the middle region. Both the left and the right CAP has the same range (Δx). The accuracy of the approach can be improved by increasing the range of the complex potentials[62] which decreases reflections.

In the calculations we need the matrix representation of the CAP in the left and in the right. These matrices are denoted by W_L and W_R and defined in the Appendix.

The Hamiltonian matrix when adding the complex potentials takes the form

$$H = \begin{pmatrix} H'_L & H_{LC} & 0 \\ H^\dagger_{LC} & H_C & H^\dagger_{RC} \\ 0 & H_{RC} & H'_R \end{pmatrix}, \tag{13}$$

where

$$H'_X = H_X - iW_X, \qquad (X = L, R). \tag{14}$$

Note that the complex potential starts in the lead region, therefore H_{LC} and H_{RC} are not affected by the addition of the CAP.

III. III. THE TIME-INDEPENDENT APPROACH

In the time-independent case the non-equilibrium Green's function combined with the CAP approach is used to calculate the current. The expression for the steady state current for an applied bias V_b is[1]

$$I(V_b) = \frac{2e^2}{h}\int_{-\infty}^{+\infty} T(E, V_b)\left[f(E-\mu_L) - f(E-\mu_R)\right] dE, \tag{15}$$

where μ_L and μ_R are the chemical potentials, f is the Fermi function, and $T(E, V_b)$ is the transmission probability (see Appendix A) for electrons from the left lead to right lead with energy E under bias V_b.

In the NEGF-DFT calculations the Kohn-Sham Hamiltonian of the central region subjected to a bias voltage is calculated self-consistently. Using the density matrix (defined in Appendix A) the electron density can be calculated as

$$\rho(\mathbf{r}) = \sum_{\mu,\nu} \phi^*_\mu(\mathbf{r}) \mathrm{Re}\left[(D_C)_{\mu\nu}\right] \phi_\nu(\mathbf{r}), \tag{16}$$

and the matrix elements of the Hamiltonian are evaluated using this density,

$$(H_C)_{\mu\nu} = \langle \phi_\mu | H_{KS} | \phi_\nu \rangle . \tag{17}$$

The Kohn-Sham Hamiltonian is defined as

$$H_{KS} = -\frac{\hbar^2}{2m}\nabla_{\mathbf{r}} + V_A(\mathbf{r}) + V_H[\rho](\mathbf{r}) + V_{XC}[\rho](\mathbf{r}), \tag{18}$$

where $V_A(\mathbf{r})$ is the atomic potential, $V_H[\rho](\mathbf{r})$ is the Hartree potential, and $V_{XC}(\mathbf{r})$ is the exchange-correlation potential. The pseudopotential approach is used to represent the atomic potentials $V_A(\mathbf{r})$. The exchange-correlation potential $V_{XC}(\mathbf{r})$ is constructed using the local density approximation[63], and the Hartree potential is calculated by solving the Poisson equation.

The calculation starts with the self-consistent solution for the left and right leads. Once the self-consistent density for the leads are found, H_L and H_R (are calculated

the self-energy can be evaluated[50] as shown in Appendix A. The bias potential in the leads is incorporated by adding a constant potential, $V_b/2$, to the electrostatic potential of the left lead and subtracting $V_b/2$ from the electrostatic potential of the right lead. Due to this change of the potential, the Hamiltonian of the leads has to be replaced by

$$H_L \to H_L + \frac{V_b}{2} S_L, \qquad H_R \to H_R - \frac{V_b}{2} S_R, \tag{19}$$

and similarly, the chemical potentials of the leads undergo the transformation

$$\mu_L \to \mu_L + \frac{V_b}{2}, \qquad \mu_R \to \mu_R - \frac{V_b}{2}. \tag{20}$$

In other words, the effect of the bias voltage is an energy shift in the leads.

The calculation proceeds with a self-consistent solution for the central region. The central region contains several lead boxes (see Fig. 4). The number of lead boxes is chosen so that in the outermost boxes, the self-consistent electron density and potential are identical to those of the leads. In this way the effect of the perturbation in the middle is screened and the assumptions used in setting up the block matrices (see Appendix A) are satisfied.

The solution of the central region is obtained by calculating the density self-consistently using Eqs. (18), (A32), and (16) together with the solution of the Poisson equation for the Hartree potential. The Poisson equation is solved on a real space grid with the boundary condition

$$V_H(\mathbf{r}) = V_H^L(\mathbf{r}) + \frac{V_b}{2} \quad \mathbf{r} \in \text{left boundary plane} \tag{21}$$

$$V_H(\mathbf{r}) = V_H^R(\mathbf{r}) - \frac{V_b}{2} \quad \mathbf{r} \in \text{right boundary plane} \tag{22}$$

where V_H^L and V_H^R are the Hartree potentials of the left and right leads. Periodic boundary conditions are used in the perpendicular directions.

IV. IV. THE TIME-DEPENDENT APPROACH

In this section the time-dependent transport approach will be presented. The multidomain decomposition method provides an accurate and efficient scheme for solving the time-dependent Kohn-Sham equations by real time propagation of the orbitals. The applicability of the approach has been tested in calculations of the photoabsorbtion spectra of long molecules[49].

In the TDDFT framework[19] the electronic motion is described by the following time-dependent Kohn-Sham equation (TKSE)

$$i\hbar \frac{\partial}{\partial t} \psi_i(\mathbf{r}, t) = H \psi_i(\mathbf{r}, t), \tag{23}$$

with

$$H = H_{KS} + V_{ext} \tag{24}$$

where

$$H_{KS} = -\frac{\hbar^2}{2m} \nabla_{\mathbf{r}} + V_A(\mathbf{r}) + V_H[\rho](\mathbf{r}, t) + V_{XC}[\rho](\mathbf{r}, t), \tag{25}$$

and $V_{ext}(\mathbf{r}, t)$ is the time-dependent external potential. In this study $V_{ext}(\mathbf{r}, t)$ will be the slowly turned on bias potential. The time dependence of the Kohn-Sham Hamiltonian, H_{KS}, is due to the time dependence of the electron density,

$$\rho(\mathbf{r}, t) = \sum_{i=1}^{N_{occ}} |\psi_i(\mathbf{r}, t)|^2. \tag{26}$$

By representing the electron wave function ψ_i in terms of domain basis functions ϕ_ν

$$\psi_i(\mathbf{r}, t) = \sum_k b_{i\nu}(t) \phi_\nu(\mathbf{r}) \tag{27}$$

the TKSE takes the form

$$i \frac{\partial B}{\partial t} = S^{-1} H B \tag{28}$$

where B is a matrix formed by the linear combination coefficients $b_{ik}(t)$ from Eq. (27). The formal solution of Eq. (28) is

$$B(t) = U(t, 0) B(0) = T \exp\left(-i \int_0^t S^{-1} H(t') dt' \right) B(0), \tag{29}$$

where T is the time ordering operator. In practical applications, most approaches break up the $[0, t]$ time interval into N_t time steps of size Δt and use a "small time propagator" to evolve the wave function from t to $t + \Delta t$. Δt is chosen to be sufficiently small so that the potential can be treated as constant in time over the time step. The time propagation using the short time propagator

$$U(t + \Delta t, t) = \exp\left(-i S^{-1} H(t) \Delta t \right), \tag{30}$$

can be written as

$$U(t, 0) \simeq \prod_{n=0}^{N_t - 1} U((n+1)\Delta t, n \Delta t), \tag{31}$$

where $\Delta t = \frac{t}{N_t}$. Various techniques have been developed[42,44,64–68] to approximate the exponential operator in Eq. (30); in this work we use the Crank-Nicholson method. The coefficients between time steps n and $n+1$ are related by the equation

$$B^{n+1} = \frac{S - iH(t_n)\frac{\Delta t}{2}}{S + iH(t_n)\frac{\Delta t}{2}} \; B^n. \tag{32}$$

The Crank-Nicholson method is unitary, strictly preserving the orthonormality of the states for an arbitrary time evolution. For time-independent Hamiltonians it is also explicitly time reversal invariant, and exactly conserves energy. In practice, with a suitable choice of Δt, the energy is satisfactorily conserved even when the Hamiltonian changes with time. One can increase the stability of the solution by including more terms of the expansion in the numerator and denominator of the Crank-Nicholson operator[69].

As shown in Section II.A, the Hamiltonian and the overlap matrices will be block tridiagonal in the domain decomposition representation facilitating the efficient calculation of the inverse of $(S + iH\frac{\Delta t}{2})$ for the time propagation of the wave function[49].

In the time-dependent approach we first calculate the ground state Kohn-Sham eigenstates,

$$\psi_i(\mathbf{r}, 0) = \sum_\nu b_{i\nu}(0)\phi_\nu(\mathbf{r}) \quad (i = 1, \ldots, N_{occ}). \tag{33}$$

These orbitals are time propagated using Eq. (32). At $t = 0$ the bias potential is turned on slowly with a ramping function. The bias potential is defined as

$$V_{ext}(\mathbf{r}, t) = \begin{cases} f(t)\frac{V_b}{2} & \mathbf{r} \in \text{left lead} \\ 0 & \mathbf{r} \in \text{central region} \\ -f(t)\frac{V_b}{2} & \mathbf{r} \in \text{left lead} \end{cases} \tag{34}$$

with the ramping function

$$f(t) = \begin{cases} t/\tau & t \leq \tau \\ 1 & \tau < t \end{cases}. \tag{35}$$

Once the bias potential is turned on, the electrons start to move from left to right. In a finite simulation box the electron current quickly reaches the boundary and gets reflected producing standing waves leading to spurious results. One can avoid these effects by stopping the simulation before the current reaches the boundary but this restricts the simulation to short times. In the present work, as it is described in Section II.3, a CAP is added to Hamiltonian in the leads to absorb the outgoing waves. This allows long time simulation without reflections. In the region where the CAP is zero the wave function of the system is unchanged and can be used to calculate the desired physical properties. In the region where the CAP is nonzero the wave function is absorbed and distorted (see Fig. 3). In most applications of CAP this does not cause any problems because one is only interested in the wave function in the region where there is no complex potential.

In the present application, however, the CAP causes electron density depletion in the leads which, through the Hartree and exchange correlation potentials, would affect the result even in the region where the CAP is zero (see Fig. 3). We have tested two approaches to avoid this effect. In the first approach, which was proposed in Ref.[47], the CAP only acts on the orbitals which are unoccupied in the ground state of the system. To this end the CAP is multiplied by a projector P,

$$W \to PWP, \tag{36}$$

which projects into the space of unoccupied orbitals,

$$P = 1 - \sum_{i=1}^{N_{occ}} |\psi_i(\mathbf{r}, 0)\rangle\langle\psi_i(\mathbf{r}, 0)|, \tag{37}$$

assuring that electrons which are not excited above the Fermi level of the leads are not absorbed. Using this projector corrected CAP, the occupied states in the lead remain unperturbed and the electrostatic and exchange correlation of the lead does not change.

In the second approach the density is only updated in the region where the CAP is zero and the the potential is kept constant in the region where the CAP is nonzero. This is basically the same restriction as is used in the time-independent calculation. In our test calculations both of these approaches gave nearly identical results. The first approach is computationally less efficient because the projector destroys the block diagonal structure of the H and S matrices. In the calculations presented in this paper the second approach will be used because it is faster and more closely mimics the time-independent approach allowing better comparison.

In the time-dependent approach the current is calculated by monitoring the number of electrons in the left and right leads. This is done by defining a measurement region in the left and right lead. Denoting the the number of electrons in the left and right measurement region by $N_L(t)$ and $N_R(t)$, the number of electrons transfered from the left to the right is

$$N(t) = \frac{1}{2}(N_R(t) - N_L(t)) \tag{38}$$

and the current is the time derivative of $N(t)$,

$$I(t) = \frac{dN(t)}{dt}. \tag{39}$$

The current can also be calculated from the wave function by using the expression:

$$\mathbf{j}(\mathbf{r}, t) = \frac{e\hbar}{2mi} \sum_{i=1}^{N_{occ}} \left(\psi_i^*(\mathbf{r}, t)\nabla_{\mathbf{r}}\psi_i(\mathbf{r}, t) - \psi_i(\mathbf{r}, t)\nabla_{\mathbf{r}}\psi_i^*(\mathbf{r}, t)\right). \tag{40}$$

By integrating the x component of $\mathbf{j}(\mathbf{r}, t)$ on the $y - z$ plane in the the lead,

$$I(t) = \int_A \mathbf{j}_x(\mathbf{r}, t)dydz. \tag{41}$$

In the numerical calculations the x position of the plane where the current is calculated is usually taken in the measurement region.

An alternative possibility[70] to extract the current from the time-dependent calculations is to calculate the transmission coefficient either by using from the time propagated orbitals[71] or with the help of the NEGF formalism as described in[70] (see Eq. (23) in[70]). This approach is somewhat more complicated then the method used here.

V. V. RESULTS AND DISCUSSION

In this section numerical examples will be presented for calculation of conductance and current-voltage characteristics using the time-independent and the time-dependent approaches. A mono-atomic gold wire and two molecular junctions, a benzene-dithiolate (BDT) and a bipyridine (BPY) molecule sandwiched between Au(111) surfaces will be used as examples.

As a first test case the conductance of a mono-atomic gold chain is calculated. The transmission as a function of energy calculated by using the time-independent approach is shown in Fig. 5. The conductance is quantized and it is equal to nG_0, where n the number of open channels (the number of Bloch waves) at a given energy and $G_0 = 2e^2/h$ is the unit of the conductance.

To calculate the conductance using the time-dependent approach the current is calculated for three small voltages, $V_b = 0.005V$, $V_b = 0.01V$, and $V_b = 0.05V$. The number of electrons moved from the right from the left as function of time is shown in Fig. 6. From the slope of these curves (using eq. (39)) the current can be determined and using these currents the average conductance is 1.04 G_0. The conductance calculated by the time-independent and time-dependent approaches are in excellent agreement. The conductance of a mono-atomic gold chain has also been calculated by a time-dependent tight-binding approach[29]. The conductance value, $G = 0.99G_0$ found in that work is also in good agreement with our results.

The current as a function of time at bias voltage $V_b = 2$ V is shown in Fig. 7. The bias potential is ramped using Eq. (35) with τ=0.25 fs. After the ramping period, the current oscillates but this oscillation slowly decays and the current becomes constant. This oscillatory behavior has been observed in other time-dependent calculations[28,35] as well. Using one-dimensional model calculations (not shown here) we have carefully checked that turning on a time-independent potential with linear ramping in the time-dependent Schrödinger equation leads to steady solutions. In density functional calculations, however, the situation is more complicated because the potentials depend on the time-dependent electron density. The effect of this nonlinearity on the time dependence of the solution is not clear. In our experience, if the simulation time is long enough then with proper ramping one can reach a steady state. The problem of steady states in time-dependent density functional calculations has been the subject of numerous studies[22,72–74]. This is an open question which needs further research exploring how memory effects and the presence of bound and resonance states in the molecular junction influence the long time behavior of the wave function in time-dependent simulations.

Fig. 7 also shows the effect of the finite size of the simulation cell. The bias potential moves electrons from the left to the right. In principle the lead is an infinite reservoir of electrons. In the model calculation, however, the number of electrons in the left lead gradually decreases. After some time this leads to an electron deficiency and the current starts to decrease (see Fig. 7). The finite size of the simulation cell presents a limitation for the time-dependent simulation; one can only continue the simulation while the charge deficiency in the left lead is negligible. Fig. 7 shows that by increasing the size of the system this finite size effect can be delayed and the calculation can be continued for a longer time.

Next we calculate the current as a function of bias voltage for molecular junctions using two different molecules sandwiched between gold electrodes. The first molecule, the benzene-dithiolate (BDT) has a smaller (1.45 eV) HOMO-LUMO gap, and the second molecule, the bipyridine has a larger (3.05 eV) HOMO-LUMO gap (the HOMO-LUMO gap is calculated with TDDFT using Casida's method[75]). The geometry of the molecular junctions is taken from Ref.[76]. To make the calculations computationally feasible the $\mathbf{k}_\parallel$ points are sampled only by using the Γ point.

In the calculations presented in this paper each lead domain contains three layers of gold atoms. The central region has five domains: two lead domains in the left, two in the right, and one domain containing the molecule and one layer of gold (see Fig. 4). The extra layer of gold is needed to make the system symmetric and the lead in the left and right identical. The lead region contains 6 domains in both sides. The leads are large enough so that the calculated current does not change by further increasing the number of domains.

The first example is the gold-BDT-gold junction which has been a prototypical example of molecular junctions and attracted intense theoretical[8,76–85] and experimental[86–90] interest.

The zero bias transmission coefficient calculated by the time-independent approach is shown in Fig. 8. The transmission curve is in good overall agreement with the results presented in Ref.[76]. There are two large peaks in the transmission: one is about 1 eV below the Fermi energy, while the second is about 3 eV above. The conductance at the Fermi energy is 0.20 G_0, in a good agreement with the results (0.24 G_0 and 0.28 G_0) presented in Ref.[76]. The calculated current-voltage characteristics are shown in Fig. 13.

In the time-dependent approach the Kohn-Sham orbitals (Eq. (33)) calculated for V_b=0 V are time propagated to to calculate the time-dependent wave function for a given bias voltage. The number of electrons moved from the left to right electrode is shown in Fig. 9 for the gold-BDT-gold junction for five different voltages. The

current calculated using eq. (41) is shown in Fig. 10. The current extracted from using Fig. 9 using Eq. (39) and the current shown in Fig. 10 are in good agreement. The charge transfer shows a linear increase of charge on the right electrode after the bias voltage is turned on with the linear ramping. After the ramping the current has a short transient and approaches the steady state. For higher bias voltages the current remains more oscillatory. This makes the value of the current somewhat ambiguous and, as the computational cost does not allow us to continue the simulations until the oscillations completely decay, we limit the calculations to small $V_b < 3V$ bias voltages. The current-voltage characteristics obtained by the time-independent approach are shown in Fig. 13.

The currents calculated by the time-dependent and time-independent approaches, except for very low bias voltages, are significantly different. To explore the origin of this difference we have compared the potential and the density calculated by the time-dependent and time-independent approaches in Fig. 11. Fig. 11.b shows the difference of the electron density at finite bias and the electron density at equilibrium ($V_b = 0V$). The change of electron density is smaller in the time-dependent approach than in the time-independent one. The bias seems to move electrons from the left sulfur atom to the right sulfur atom. In the time-independent approach more electrons are moved towards the right lead by the bias voltage. As a consequence, the voltage drop across the junction is smoother in the time-dependent case than in the time-independent one. The smoother potential leads to higher transmission probability allowing larger current through the molecule. The reason behind the different densities and potentials produced by the two approaches is the fact that the non-equilibrium part of the density (the part of the density induced by the bias voltage) is calculated from different Hamiltonians. This question will be addressed further by comparing the spectrum of the two Hamiltonians. This example only shows that the difference in the Hamiltonians leads to different currents, but there is no rule saying that the time-dependent approach yields larger current. The particular results are probably different for different systems and one expects that it strongly depends on the energy levels of the molecule, as well as the coupling between the molecule and the leads.

Fig. 12 shows the average potential at t=1 fs. Similar to the time-independent case, the change of potential due to the bias voltage is only significant around the molecular junction in the time-dependent calculations. Fig. 12 shows that the potential is only affected by the bias voltage up to 3-4 gold layers (between -10 and 10 Å).

Our next example is the gold-BPY-gold junction. The geometry of the system is taken from Ref.[76]. The transmission coefficient as a function of energy for the gold-BPY-gold structure is shown is Fig. 14. This system has been subject of study by various research groups experimentally[91] and theoretically[76,92–96]. The theoretical calculations have found that the transport properties very strongly depend on the details of the contact geometry. The calculated zero bias transmission coefficient (see Fig. 14) is in good agreement with the results presented in Ref.[76]. The slight differences are due to the fact that only the Γ point is used in our calculations.

The current as a function of the applied voltage is shown in Fig. 15. Due to the small transmission probability around the Fermi energy, the calculated current is very small for low bias voltages. This is in good agreement with both the previous calculations[92,94] and with experimental results[91]. The Fermi energy of the system is aligned about 0.5eV below the LUMO level (see Fig. 16). The current starts to increase when the bias voltage is $V_b > 0.5V$ and the transmission becomes significant through the LUMO level. Up to that point, the currents calculated by the time-dependent and time-independent approaches are nearly equal. Beyond that region there is a significant difference between the two results. Due to the nonzero transmission around the Fermi energy in the BDT case, the current is larger for BDT than for BPY even for small bias voltages (see Fig. 13).

As we have seen, the currents calculated by the time-dependent and time-independent approaches are significantly different. In the two cases studied in this paper the time-dependent approach predicts a larger current than the time-independent one. One of the reasons for this difference is that in the time-independent case the current is calculated from the transmission function which is based on the ground state Kohn-Sham Hamiltonian and the excited states are approximated by the unoccupied Kohn-Sham eigenstates. In the time-dependent case the excited states are accessed through TDDFT providing a better description of the current for finite bias voltages. Figs. 16 and 17 show the difference between the energies of the unoccupied Kohn-Sham states and the energies of the excited states calculated by TDDFT using Casida's method[75] for the BDT and BPY molecules. The BDT has a smaller HOMO-LUMO gap than the BPY. Both ground state DFT and TDDFT predict similar HOMU-LUMO gaps for both molecules. The energies of the higher states, however, are different in the two approaches. The similarity of the currents calculated for BPY (see Fig. 15) in the low bias voltage regime can probably be attributed to the fact that the HOMO-LUMO gap is large in both approaches. The higher excited states are predicted to be different by the two approaches and the calculated current is different as well. Similar arguments are true for the BDT junction, except for the fact that in the BDT case the HOMO-LUMO gap is smaller causing the current to be different everywhere.

VI. SUMMARY

The multidomain decomposition method together with the complex potential approach has been used to calculate the current as a function of voltage in molecular junctions using the time-dependent DFT and the time-

independent NEGF-DFT method. The results of the time-independent approach for molecular junctions and for a mono-atomic gold wire are in good agreement with previous calculations. The results of the time-dependent calculations are significantly different from the static NEGF-DFT results. This difference can mostly be attributed to the fact that the TDDFT approach accesses the excited states of the system while NEGF-DFT is restricted to the ground state single particle orbitals.

In the present work the local density approximation (LDA) is used for the exchange-correlation potential. An obvious way to improve the calculations is to use better exchange-correlation potentials. Intense research is already devoted to this problem. The effect of the self-interaction correction is investigated in[97,98] and the problem of the lack of derivative discontinuity in LDA-based calculations has been illustrated. The impact of exchange-correlation effects on the current-voltage characteristics of a molecular junction has been studied in Ref.[99]. More rigorous approaches based on exact exchange[100] would be desirable, but their implementation is tedious[101]. Time-dependent calculations going beyond the adiabatic LDA level are a necessary further step for better description of the electron transport in nanostructures.

The present work is concentrated on the study of electron transport in the presence of a time-independent external bias potential. The presented implementation of the time-dependent approach provides an efficient framework for transport calculations with time-dependent external potentials as well. Results of such calculations will be reported in the future.

In the present work, the infinite open quantum system has been transformed into a finite closed system, which is an efficient and cheap way of to calculate electron transport in molecular junctions. The calculation of electron current using TDDFT in open quantum systems is a very active research area[39,70,102–104]. There are numerous other approaches have been proposed to address this problem including the extension of TDDFT to open systems using a Liouville-master equation[39,102,103], description of the environment introducing quantum Drude friction[104] and using a stochastic Schrödinger-equation to tackle quantum dynamics[105]. A particularly attractive feature of some of these approaches that they allow one to go beyond TDDFT and use current density functional theory[106].

This work is supported by NSF Grants No. ECCS0925422 and CMMI0927345.

Appendix A: Definition of the matrices used in the time-independent calculations

In this Appendix we will define the matrices used in the time-independent transport calculations. The definitions used in this paper conform with those in the literature[2,3]. The purpose of this Appendix is to make the paper self-contained and to connect the multidomain expression presented in Eq. (3) to the standard transport expression of Eq. (6).

In transport calculations, the left and right leads consist of periodically repeated cells. The domains in the leads are chosen to contain one or more cells. The number of cells included in the domains is selected in such a way that the Hamiltonian and the overlap matrices only connect adjacent boxes. As the boxes in the leads are identical, so are the H_{Bi}, H_{Ai}, and S_{Bi} and S_{Ai} matrices. Denoting the number of domains in the left and right and center by n_L, n_R, and n_C, respectively, we can define

$$H_{Bi} = H_B^L, \quad H_{Ai} = H_A^L, \quad S_{Bi} = S_B^L, \quad S_{Ai} = S_A^L, \tag{A1}$$

for $(i = 1, \ldots, n_L)$

$$H_{Bi} = H_B^R, \quad H_{Ai} = H_A^R, \quad S_{Bi} = S_B^R, \quad S_{Ai} = S_A^R, \tag{A2}$$

for $i = n_L + n_C + 1, \ldots, N$. In the central region no such simplification is possible, and we have

$$H_{Bi} = H_{Bi}^C, \quad H_{Ai} = H_{Ai}^C, \quad S_{Bi} = S_{Bi}^C, \quad S_{Ai} = S_{Ai}^C, \tag{A3}$$

for $i = n_L + 1, \ldots, n_L + n_C$. Using this notation, the Hamiltonian and the overlap matrices of the left and right leads are

$$H_L = \begin{pmatrix} H_B^L & H_A^{L\dagger} & 0 & \ldots & 0 & 0 \\ H_A^L & H_B^L & H_A^{L\dagger} & \ldots & 0 & 0 \\ 0 & H_A^L & H_B^L & \ldots & 0 & 0 \\ \vdots & \vdots & \vdots & \ddots & \vdots & \vdots \\ 0 & 0 & 0 & \ldots & H_B^L & H_A^{L\dagger} \\ 0 & 0 & 0 & \ldots & H_A^L & H_B^L \end{pmatrix}, \tag{A4}$$

$$S_L = \begin{pmatrix} S_B^L & S_A^{L\dagger} & 0 & \ldots & 0 & 0 \\ S_A^L & S_B^L & S_A^{L\dagger} & \ldots & 0 & 0 \\ 0 & S_A^L & S_B^L & \ldots & 0 & 0 \\ \vdots & \vdots & \vdots & \ddots & \vdots & \vdots \\ 0 & 0 & 0 & \ldots & S_B^L & S_A^{L\dagger} \\ 0 & 0 & 0 & \ldots & S_A^L & S_B^L \end{pmatrix}, \tag{A5}$$

$$H_R = \begin{pmatrix} H_B^R & H_A^{R\dagger} & 0 & \ldots & 0 & 0 \\ H_A^R & H_B^R & H_A^{R\dagger} & \ldots & 0 & 0 \\ 0 & H_A^R & H_B^R & \ldots & 0 & 0 \\ \vdots & \vdots & \vdots & \ddots & \vdots & \vdots \\ 0 & 0 & 0 & \ldots & H_B^R & H_A^{R\dagger} \\ 0 & 0 & 0 & \ldots & H_A^R & H_B^R \end{pmatrix}, \tag{A6}$$

$$S_R = \begin{pmatrix} S_B^R & S_A^{R\dagger} & 0 & \ldots & 0 & 0 \\ S_A^R & S_B^R & S_A^{R\dagger} & \ldots & 0 & 0 \\ 0 & S_A^R & S_B^R & \ldots & 0 & 0 \\ \vdots & \vdots & \vdots & \ddots & \vdots & \vdots \\ 0 & 0 & 0 & \ldots & S_B^R & S_A^{R\dagger} \\ 0 & 0 & 0 & \ldots & S_A^R & S_B^R \end{pmatrix}. \tag{A7}$$

In the central region the matrices are defined as

$$H_C = \begin{pmatrix} H^C_{B1} & H^{C\dagger}_{A2} & 0 & 0 & \dots \\ H^C_{A2} & H^C_{B2} & H^{C\dagger}_{A3} & 0 & \dots \\ & & & & H^{C\dagger}_{AN_C} \\ 0 & \dots & & H^C_{AN_C} & H^C_{BN_C} \end{pmatrix} \tag{A8}$$

and

$$S_C = \begin{pmatrix} S^C_{B1} & S^{C\dagger}_{A2} & 0 & 0 & \dots \\ S^C_{A2} & S^C_{B2} & S^{C\dagger}_{A3} & 0 & \dots \\ & & & & S^{C\dagger}_{AN_C} \\ 0 & \dots & & S^C_{AN_C} & S^C_{BN_C} \end{pmatrix}. \tag{A9}$$

The coupling matrices between the leads and the central region are

$$H_{LC} = \begin{pmatrix} 0 & 0 & \dots & 0 \\ 0 & 0 & \dots & 0 \\ 0 & 0 & \dots & 0 \\ \vdots & \vdots & \ddots & \vdots \\ 0 & 0 & \dots & 0 \\ H^{LC} & 0 & \dots & 0 \end{pmatrix}, \tag{A10}$$

$$H_{RC} = \begin{pmatrix} 0 & \dots & 0 & H^{RC} \\ 0 & \dots & 0 & 0 \\ 0 & \dots & 0 & 0 \\ \vdots & \ddots & \vdots & \vdots \\ 0 & \dots & 0 & 0 \\ 0 & \dots & 0 & 0 \end{pmatrix}. \tag{A11}$$

where

$$H^{LC} = H_{An_L+1}, \qquad S^{LC} = S_{An_L+1}, \tag{A12}$$

$$H^{RC} = H_{An_L+n_C+1}, \qquad S^{RC} = S_{An_L+n_C+1}. \tag{A13}$$

Using this notation, the Hamiltonian and the overlap matrices can be written as

$$H = \begin{pmatrix} H_L & H_{LC} & 0 \\ H^\dagger_{LC} & H_C & H^\dagger_{RC} \\ 0 & H_{RC} & H_R \end{pmatrix}, \tag{A14}$$

$$S = \begin{pmatrix} S_L & S_{LC} & 0 \\ S^\dagger_{LC} & S_C & S^\dagger_{RC} \\ 0 & S_{RC} & S_R \end{pmatrix}. \tag{A15}$$

The matrix representations of the CAP in the left and right leads are

$$W_L = \begin{pmatrix} W^L_{Bn_L} & W^{L\dagger}_{An_L-1} & 0 & \dots & 0 & 0 \\ W^L_{An_L-1} & W^L_{Bn_L-1} & W^{L\dagger}_{An_L-2} & \dots & 0 & 0 \\ 0 & W^L_{An_L-2} & W^{BL}_{n_L-2} & \dots & 0 & 0 \\ \vdots & \vdots & \vdots & \ddots & \vdots & \vdots \\ 0 & 0 & 0 & \dots & W^L_{B2} & W^{L\dagger}_{A1} \\ 0 & 0 & 0 & \dots & W^L_{A1} & W^L_{B1} \end{pmatrix}, \tag{A16}$$

$$W_R = \begin{pmatrix} W^R_{B1} & W^{R\dagger}_{A2} & 0 & \dots & 0 & 0 \\ W^R_{A2} & W^R_{B2} & W^{R\dagger}_{A3} & \dots & 0 & 0 \\ 0 & W^R_{B3} & W^R_{B3} & \dots & 0 & 0 \\ \vdots & \vdots & \vdots & \ddots & \vdots & \vdots \\ 0 & 0 & 0 & \dots & W^R_{Bn_R-1} & W^{R\dagger}_{Bn_R} \\ 0 & 0 & 0 & \dots & W^R_{Bn_R} & W^R_{Bn_R} \end{pmatrix}, \tag{A17}$$

where the block matrices, W^L_{Xi} and W^R_{Xi} correspond to the principal layers and thus the block matrices H^L_X and H^R_X of the Hamiltonian of the lead ($X = A, B$). Using these CAP matrices the Hamiltonians of the leads are defined as

$$H'_X = H_X - iW_X, \quad (X = L, R). \tag{A18}$$

Next, we define the Green's functions of the different partitions. The Green's functions of the leads are

$$g_X(E) = ((E + i\epsilon^+)S_X - H'_X)^{-1} \qquad X = L, R \tag{A19}$$

(where ϵ^+ is an infinitesimally small positive number). The Green's function of the central region is

$$G_C(E) = ((E + i\epsilon^+)S_C - H_C - \Sigma_L(E) - \Sigma_R(E))^{-1}. \tag{A20}$$

where

$$\Sigma_L = (ES_{LC} - H_{LC})^\dagger \, g_L \, (ES_{LC} - H_{LC}), \tag{A21}$$

and

$$\Sigma_R = (ES_{RC} - H_{RC})^\dagger \, g_R \, (ES_{RC} - H_{RC}). \tag{A22}$$

are the self-energy matrices of the leads. Using the block matrix form of the leads' Green's functions

$$g_L = \begin{pmatrix} g^L_{11} & g^{L\dagger}_{12} & \dots & \dots & \dots & g^{L\dagger}_{n_1 L} \\ g^L_{12} & g^L_{22} & g^{L\dagger}_{23} & \dots & \dots & \dots \\ g^L_{13} & g^L_{23} & g^L_{33} & \dots & \dots & \dots \\ \vdots & \vdots & \vdots & \ddots & \vdots & \vdots \\ \vdots & \vdots & \vdots & \dots & g^L_{n_L-1 n_L-1} & g^{L\dagger}_{n_L-1 n_L} \\ g^L_{1 n_L} & \dots & \dots & \dots & g^L_{n_L-1 n_L} & g^L_{n_L n_L} \end{pmatrix}, \tag{A23}$$

and

$$g_R = \begin{pmatrix} g^R_{11} & g^{R\dagger}_{12} & \dots & \dots & \dots & g^{R\dagger}_{n_R 1} \\ g^R_{12} & g^R_{22} & g^{R\dagger}_{23} & \dots & \dots & \dots \\ g^R_{13} & g^R_{23} & g^R_{33} & \dots & \dots & \dots \\ \vdots & \vdots & \vdots & \ddots & \vdots & \vdots \\ \vdots & \vdots & \vdots & \dots & g^R_{n_R-1 n_R-1} & g^{R\dagger}_{n_R-1 n_R} \\ g^R_{1 n_R} & \dots & \dots & \dots & g^R_{n_R-1 n_R} & g^R_{n_R n_R} \end{pmatrix}, \tag{A24}$$

and the special sparse structure of H_{LC} and H_{RC} the

sigma matrices become

$$\Sigma_L = \begin{pmatrix} \sigma_L & \dots & 0 & 0 \\ 0 & \dots & 0 & 0 \\ 0 & \dots & 0 & 0 \\ \vdots & \ddots & \vdots & \vdots \\ 0 & \dots & 0 & 0 \\ 0 & \dots & 0 & 0 \end{pmatrix}, \tag{A25}$$

and

$$\Sigma_R = \begin{pmatrix} 0 & \dots & 0 & 0 \\ 0 & \dots & 0 & 0 \\ 0 & \dots & 0 & 0 \\ \vdots & \ddots & \vdots & \vdots \\ 0 & \dots & 0 & 0 \\ 0 & \dots & 0 & \sigma_R \end{pmatrix}, \tag{A26}$$

with

$$\sigma_L = \left((E+i\epsilon^+)S^{LC} - H^{LC}\right)^\dagger g^L_{n_L n_L} \left((E+i\epsilon^+)S^{LC} - H^{LC}\right) \tag{A27}$$

$$\sigma_R = \left((E+i\epsilon^+)S^{RC} - H^{RC}\right)^\dagger g^R_{11} \left((E+i\epsilon^+)S^{RC} - H^{LR}\right). \tag{A28}$$

Both Σ_L and Σ_R are $N_C \times N_C$ matrices with only a single nonzero block matrix.

Lastly, using the self-energies and the Green's functions we can define the transmission probability and the charge density matrix. The transmission probability is related to Green's functions by[1]

$$T(E, V_b) = \mathrm{Tr}\left[\Gamma_L(E) G_C(E) \Gamma_R(E) G_C^\dagger(E)\right], \tag{A29}$$

where

$$\Gamma_{L,R}(E) = i\left(\Sigma_{L,R}(E) - [\Sigma_{L,R}(E)]^\dagger\right) \tag{A30}$$

represents the coupling at energy E between the central region and the leads.

The electron density can be calculated from the density matrix of the central region

$$D_C = \frac{1}{2\pi}\int_{-\infty}^{+\infty} dE \left[G_C(E)\Gamma_L(E)G_C^\dagger(E) f(E-\mu_L) + G_C(E)\Gamma_R(E)G_C^\dagger(E) f(E-\mu_R)\right] \tag{A31}$$

$$= -\frac{1}{\pi}\int_{-\infty}^{+\infty} dE \mathrm{Im}\left[G_C(E) f(E-\mu_L)\right] \tag{A32}$$

$$+\frac{1}{2\pi}\int_{-\infty}^{+\infty} dE \left[G_C(E)\Gamma_R(E)G_C^\dagger(E)\right] \times \left[f(E-\mu_R) - f(E-\mu_L)\right].$$

The first integral is analytic (all poles of $G_C(E)$ are on the real axis), and the integral can be evaluated by complex contour integration. The second integrand is not analytic, and it must be evaluated by integrating very close to the real axis using a very fine energy mesh.

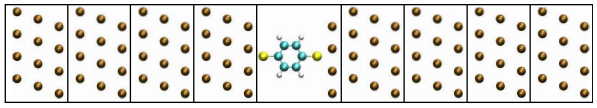

FIG. 1: Domain decomposition.

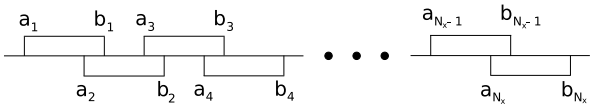

FIG. 2: Intervals in the x direction.

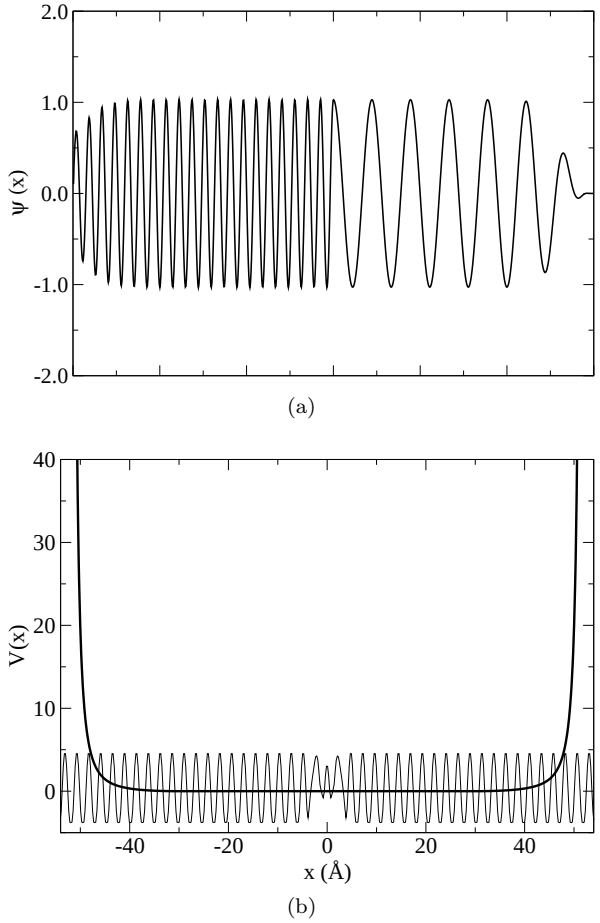

FIG. 3: Top panel: Real part of a scattering wave function in a complex absorbing potential. The wave function is calculated for a step potential and it is equal to the analytical solution in the [-20Å ,20Å] region where the CAP is zero. The nonzero CAP absorbs the wave function and the wave function gradually decays to zero. Bottom panel: Imaginary part of the complex absorbing potential (thick solid line) and self-consistent potential (thin solid line) for a gold-benzene-dithiolate-gold junction. The potential is obtained by averaging the self-consistent potential on the plane perpendicular to the transport direction.

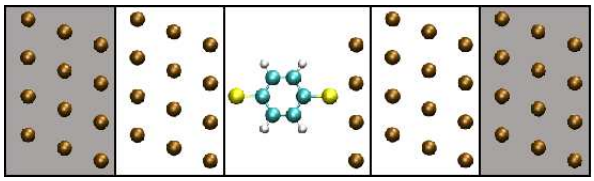

FIG. 4: Central region. The size of the system is chosen in such a way that the self consistent solution in the shaded boxes is identical to the self-consistent solution of the lead boxes.

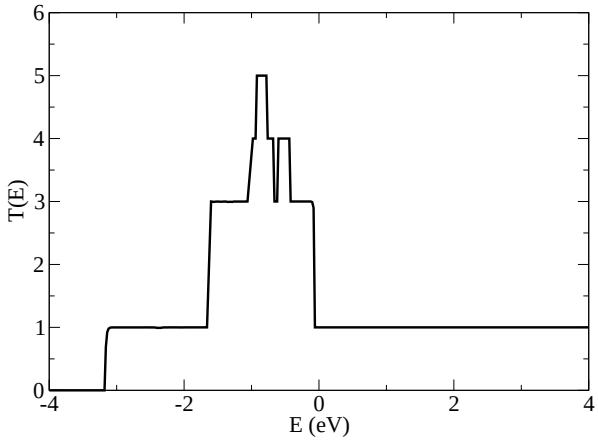

FIG. 5: Conductance of a gold nanowire as a function of the energy.

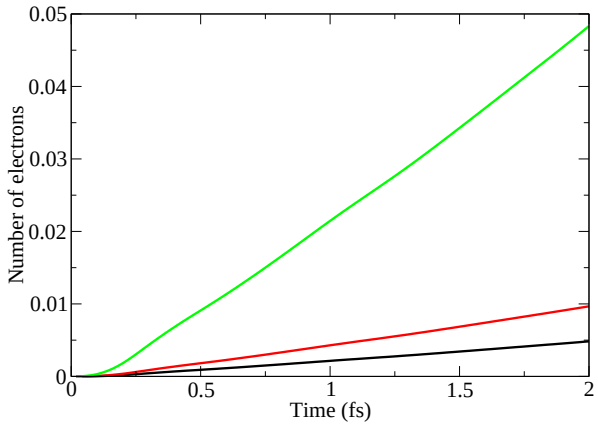

FIG. 6: Number of electrons moved from the left to the right as a function of time for three different bias voltages, $V_b = 0.005V$ (lower line), $V_b = 0.01V$ (middle line), and $V_b = 0.05V$ (upper line).

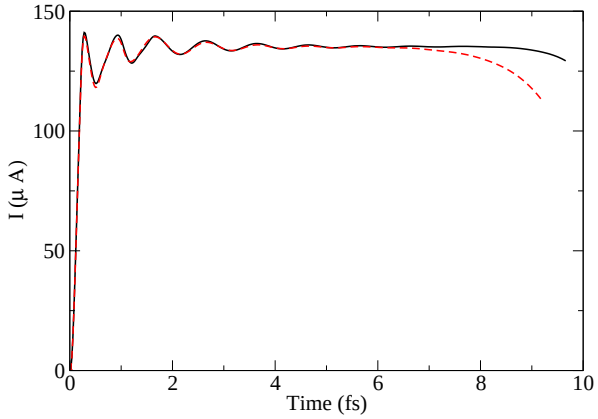

FIG. 7: Current as function of time in gold nanowires. The applied bias voltage is V_b=2 V. The length of the nanowires are 180 Å(dashed line) and 230 Å(solid line).

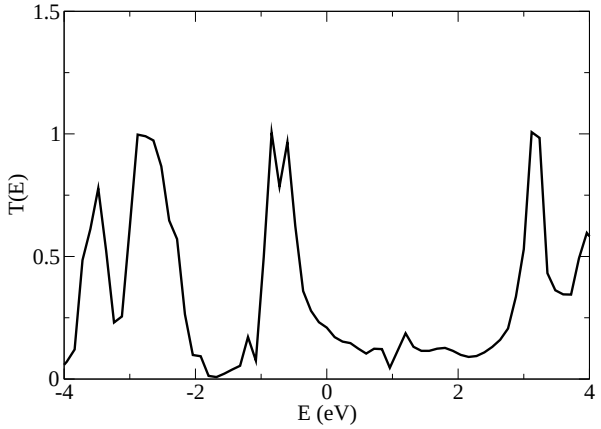

FIG. 8: Transmission as a function of energy for the gold-benzene-dithiolate-gold junction.

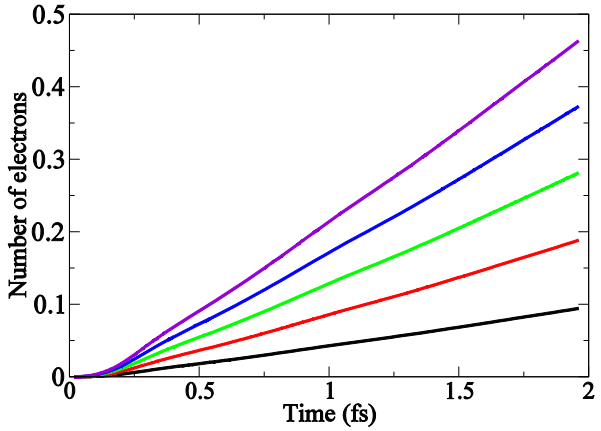

FIG. 9: The number of electrons moved from the left to right electrode as a function of time for the gold-BDT-gold junction for five different bias voltages. The lowest curve corresponds to $V_b = 1V$, and the bias voltage is increased by $1V$ for the successive curves.

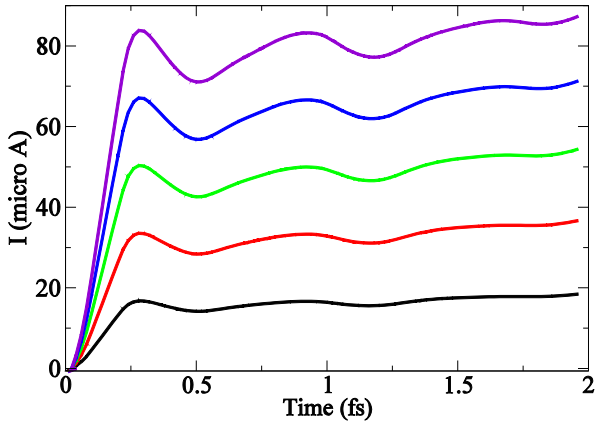

FIG. 10: Current as a function of time for the gold-BDT-gold junction for five different bias voltages. The lowest curve corresponds to $V_b = 1V$, and the bias voltage is increased by $1V$ for the successive curves.

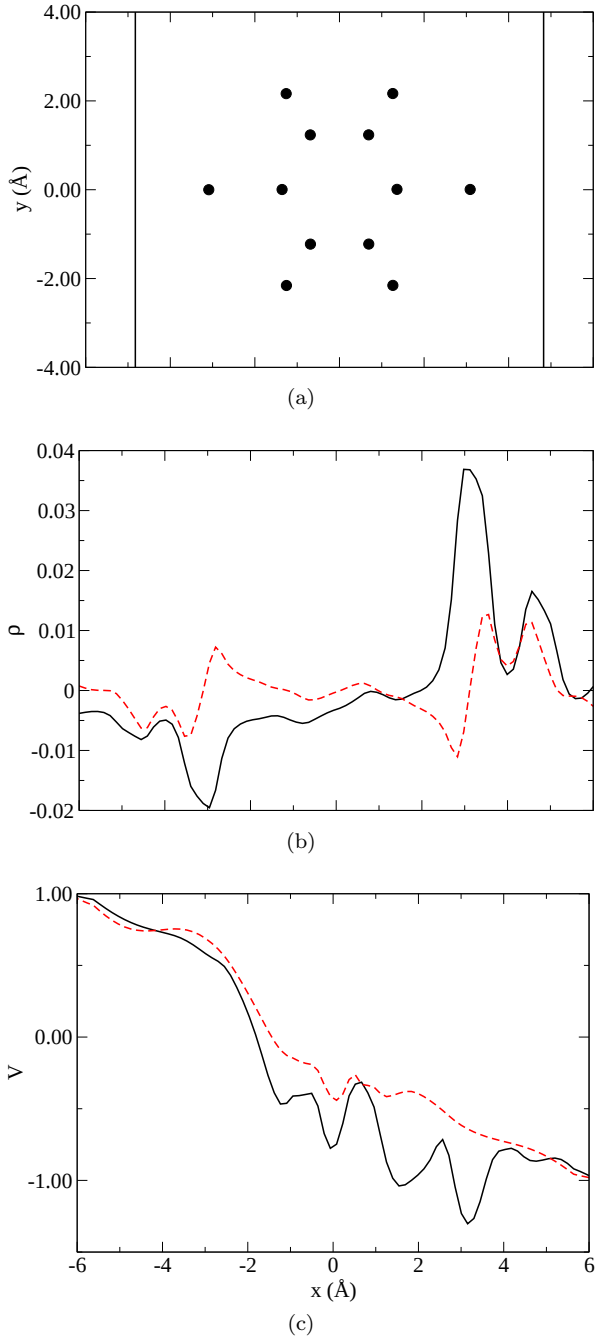

FIG. 11: Change of density (middle panel) and potential (bottom panel) in a gold-benzene-dithiolate-gold junction in the time-independent (solid line) and time-dependent (dashed line) calculation. The density (potential) is calculated by averaging the difference of the densities (potentials) at V_b=2 V and $V_b = 0$ V. The density and the potential is averaged over the y-z plane. The top panel shows the position of the atoms. The two vertical lines show the position of the first gold layer (see also Fig. 4).

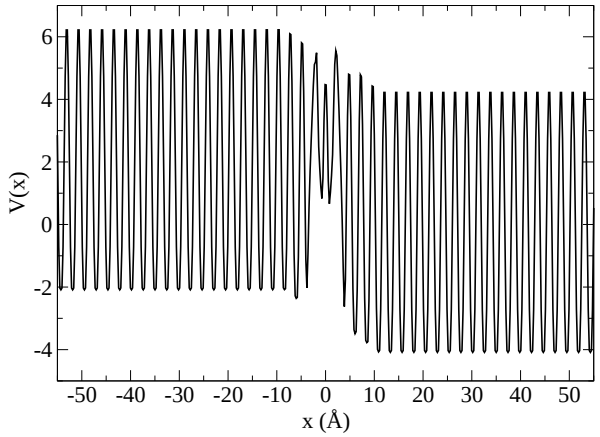

FIG. 12: Potential of the gold-benzene-dithiolate-gold junction calculated by the time-dependent approach at t=1 fs. The bias voltage is V_b=3 V. The potential shown on the figure is abtained by averaging the self-consistent potential over the y-z plane.

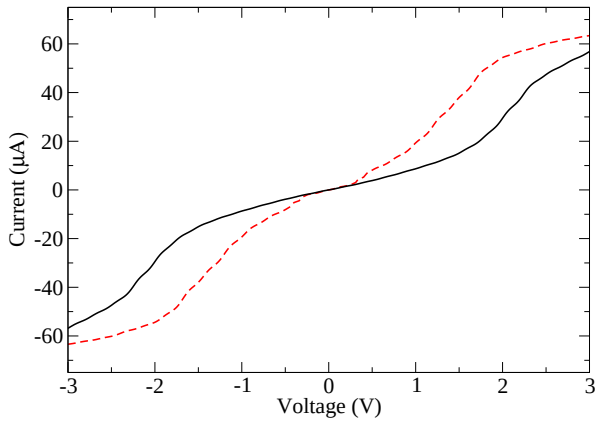

FIG. 13: Current as a function of bias voltage for the gold-benzene-dithiolate-gold junction calculated by the time-independent (solid line) and time-dependent (dashed line) approaches.

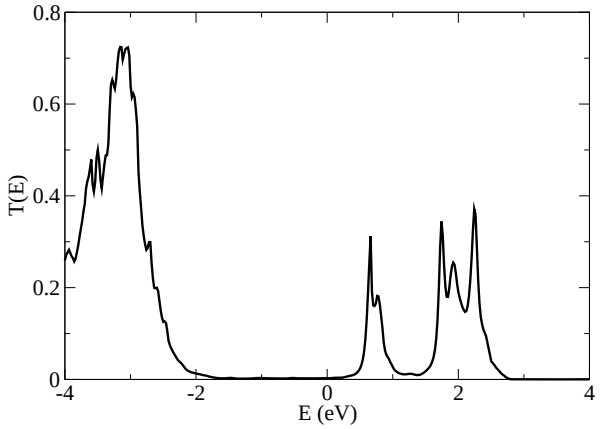

FIG. 14: Transmission as a function of energy for the gold-bipyridine-gold junction.

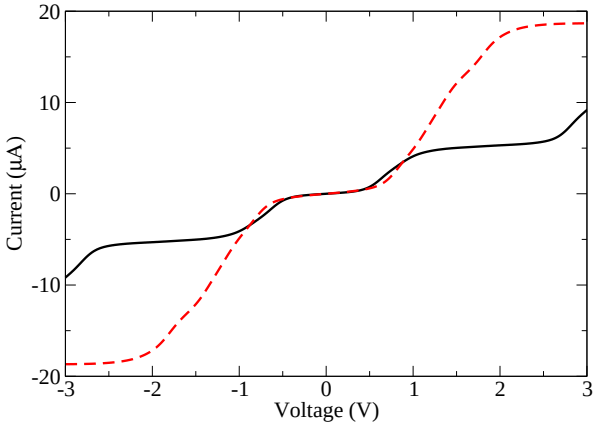

FIG. 15: Current as a function of bias voltage for the gold-bipyridine-gold junction calculated by the time-independent (solid line) and time-dependent (dashed line) approaches.

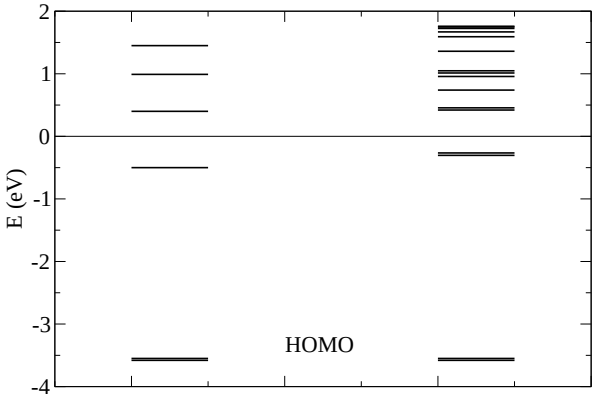

FIG. 16: Excited state spectrum of an isolated bipyridine molecule. The left side corresponds to the energies of the unoccupied the Kohn-Sham orbitals, the right hand side shows the excited state energies calculated by the TDDFT. The grey line at $E = 0$ is the Fermi energy of the gold lead. The the Fermi level and the molecular energies are aligned by equalizing the vacuum potentials of the isolated molecule and the semi-infinite lead.

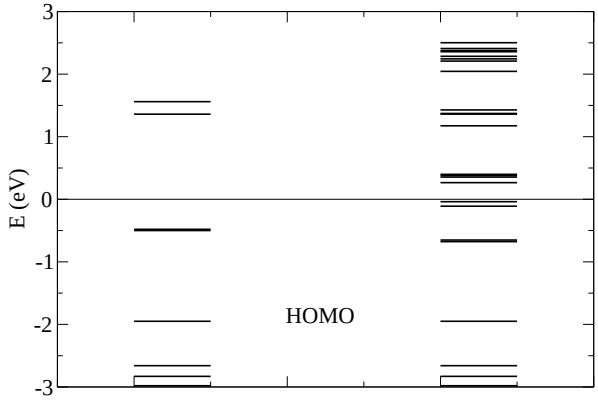

FIG. 17: Excited state spectrum of a benzene-dithiol molecule. The left side corresponds to the energies of the unoccupied the Kohn-Sham orbitals, the right hand side shows the excited state energies calculated by the TDDFT. The grey line at $E = 0$ is the Fermi energy of the gold lead. See also the caption of Fig. 16.

[1] S. Datta, *Electronic transport in mesoscopic systems* (Cambridge University Press, 1997).
[2] Y. Xue, S. Datta, and M. A. Ratner, J. Chem. Phys. **115**, 4292 (2001).
[3] M. Di Ventra, *Electrical Transport in Nanoscale Systems* (Cambridge University Press, 2008).
[4] W. Kohn and L. J. Sham, Phys. Rev. **140**, A1133 (1965).
[5] J. M. Soler *et al.*, Journal of Physics: Condensed Matter **14**, 2745 (2002).
[6] S. V. Faleev, F. m. c. Léonard, D. A. Stewart, and M. van Schilfgaarde, Phys. Rev. B **71**, 195422 (2005).
[7] J. J. Palacios, A. J. Pérez-Jiménez, E. Louis, E. San-Fabián, and J. A. Vergés, Phys. Rev. Lett. **90**, 106801 (2003).
[8] K. Stokbro, J. Taylor, M. Brandbyge, J. L. Mozos, and P. Ordejn, Computational Materials Science **27**, 151 (2003).
[9] E. G. Emberly and G. Kirczenow, Phys. Rev. B **64**, 235412 (2001).
[10] J. Taylor, H. Guo, and J. Wang, Phys. Rev. B **63**, 245407 (2001).
[11] M. B. Nardelli, J.-L. Fattebert, and J. Bernholc, Phys. Rev. B **64**, 245423 (2001).
[12] K. Thygesen and K. Jacobsen, Chemical Physics **319**, 111 (2005), Molecular Charge Transfer in Condensed Media - from Physics and Chemistry to Biology and Nanoengineering in honour of Alexander M. Kuznetsov on his 65th birthday.
[13] S.-H. Ke, H. U. Baranger, and W. Yang, Phys. Rev. B **70**, 085410 (2004).
[14] P. A. Derosa and J. M. Seminario, The Journal of Physical Chemistry B **105**, 471 (2001), http://pubs.acs.org/doi/pdf/10.1021/jp003033
[15] S. Sanvito, C. J. Lambert, J. H. Jefferson, and A. M. Bratkovsky, Phys. Rev. B **59**, 11936 (1999).
[16] S. Lindsay and M. Ratner, Advanced Materials **19**, 23 (2007).
[17] Z. Zhong, N. M. Gabor, J. E. Sharping, A. L. Gaeta, and P. L. McEuen, Nat Nano **3**, 201 (2008).
[18] Y.-M. Lin *et al.*, Nano Letters **9**, 422 (2009), http://pubs.acs.org/doi/pdf/10.1021/nl803316h.
[19] E. Runge and E. K. U. Gross, Phys. Rev. Lett. **52**, 997 (1984).
[20] G. Stefanucci and C.-O. Almbladh, EPL (Europhysics Letters) **67**, 14 (2004).
[21] G. Stefanucci and C.-O. Almbladh, Phys. Rev. B **69**, 195318 (2004).
[22] S. Kurth, G. Stefanucci, C.-O. Almbladh, A. Rubio, and E. K. U. Gross, Phys. Rev. B **72**, 035308 (2005).
[23] X. Zheng, F. Wang, C. Y. Yam, Y. Mo, and G. Chen, Phys. Rev. B **75**, 195127 (2007).
[24] S.-H. Ke, R. Liu, W. Yang, and H. U. Baranger, The Journal of Chemical Physics **132**, 234105 (2010).
[25] M. D. Ventra and T. N. Todorov, Journal of Physics: Condensed Matter **16**, 8025 (2004).
[26] J. Maciejko, J. Wang, and H. Guo, Phys. Rev. B **74**, 085324 (2006).
[27] J. Yuen-Zhou, D. G. Tempel, C. A. Rodríguez-Rosario, and A. Aspuru-Guzik, Phys. Rev. Lett. **104**, 043001 (2010).
[28] C.-L. Cheng, J. S. Evans, and T. Van Voorhis, Phys. Rev. B **74**, 155112 (2006).
[29] N. Bushong, N. Sai, and M. Di Ventra, Nano Letters **5**, 2569 (2005), http://pubs.acs.org/doi/pdf/10.1021/nl0520157.
[30] A. Prociuk and B. D. Dunietz, Phys. Rev. B **78**, 165112 (2008).
[31] N. Sai, N. Bushong, R. Hatcher, and M. Di Ventra, Phys. Rev. B **75**, 115410 (2007).
[32] G. Stefanucci, S. Kurth, A. Rubio, and E. K. U. Gross, Phys. Rev. B **77**, 075339 (2008).
[33] S. Weiss, J. Eckel, M. Thorwart, and R. Egger, Phys. Rev. B **77**, 195316 (2008).
[34] P. Myöhänen, A. Stan, G. Stefanucci, and R. van Leeuwen, Phys. Rev. B **80**, 115107 (2009).
[35] X. Qian, J. Li, X. Lin, and S. Yip, Phys. Rev. B **73**, 035408 (2006).
[36] K. Burke, R. Car, and R. Gebauer, Phys. Rev. Lett. **94**, 146803 (2005).
[37] M. Koentopp, C. Chang, K. Burke, and R. Car, Journal of Physics: Condensed Matter **20**, 083203 (2008).
[38] C. G. Sanchez *et al.*, The Journal of Chemical Physics **124**, 214708 (2006).
[39] R. Gebauer and R. Car, Phys. Rev. Lett. **93**, 160404 (2004).
[40] D. Kienle, M. Vaidyanathan, and F. m. c. Léonard, Phys. Rev. B **81**, 115455 (2010).
[41] J. S. Evans, C.-L. Cheng, and T. Van Voorhis, Phys. Rev. B **78**, 165108 (2008).
[42] I. Yabana, Nakatsukasa and Bertsch, phys. stat. sol. (b) **243**, 1121 (2006).
[43] X.-M. Tong and S.-I. Chu, Phys. Rev. A **57**, 452 (1998).
[44] A. Castro, M. A. L. Marques, and A. Rubio, The Journal of Chemical Physics **121**, 3425 (2004).
[45] Y. Kawashita, T. Nakatsukasa, and K. Yabana, Journal of Physics: Condensed Matter **21**, 064222 (2009).
[46] N. Watanabe and M. Tsukada, Phys. Rev. E **65**, 036705 (2002).
[47] R. Baer, T. Seideman, S. Ilani, and D. Neuhauser, The Journal of Chemical Physics **120**, 3387 (2004).
[48] K. Varga, Phys. Rev. B **81**, 045109 (2010).
[49] V. Goncharov and K. Varga, Phys. Rev. B **submitted** (2010).
[50] J. A. Driscoll and K. Varga, Phys. Rev. B **78**, 245118 (2008).
[51] J. A. Driscoll and K. Varga, Phys. Rev. B **81**, 115412 (2010).
[52] K. Varga, Z. Zhang, and S. T. Pantelides, Phys. Rev. Lett. **93**, 176403 (2004).
[53] J. R. Chelikowsky, N. Troullier, K. Wu, and Y. Saad, Phys. Rev. B **50**, 11355 (1994).
[54] E. L. Briggs, D. J. Sullivan, and J. Bernholc, Phys. Rev. B **54**, 14362 (1996).
[55] T. L. Beck, Rev. Mod. Phys. **72**, 1041 (2000).
[56] W. H. Miller, Accounts of Chemical Research **26**, 174 (1993), http://pubs.acs.org/doi/pdf/10.1021/ar00028a007.
[57] T. Seideman and W. H. Miller, The Journal of Chemical Physics **96**, 4412 (1992).
[58] J. Muga, J. Palao, B. Navarro, and I. Egusquiza, Physics Reports **395**, 357 (2004).
[59] A. Vibok and G. G. Balint-Kurti, The Jour-

nal of Physical Chemistry **96**, 8712 (1992), http://pubs.acs.org/doi/pdf/10.1021/j100201a012.
[60] S. Brouard, D. Macias, and J. G. Muga, Journal of Physics A: Mathematical and General **27**, L439 (1994).
[61] G. Jolicard and J. Humbert, Chemical Physics **118**, 397 (1987).
[62] D. E. Manolopoulos, The Journal of Chemical Physics **117**, 9552 (2002).
[63] E. K. U. Gross and W. Kohn, Phys. Rev. Lett. **55**, 2850 (1985).
[64] H. Tal-Ezer and R. Kosloff, The Journal of Chemical Physics **81**, 3967 (1984).
[65] D. Kosloff and R. Kosloff, Journal of Computational Physics **52**, 35 (1983).
[66] S. A. Chin and C. R. Chen, The Journal of Chemical Physics **114**, 7338 (2001).
[67] X. Zhou and C. D. Lin, Phys. Rev. A **61**, 053411 (2000).
[68] D. Rocca, R. Gebauer, Y. Saad, and S. Baroni, The Journal of Chemical Physics **128**, 154105 (2008).
[69] A. Tsolakidis, D. Sánchez-Portal, and R. M. Martin, Phys. Rev. B **66**, 235416 (2002).
[70] G. Stefanucci and C.-O. Almbladh, Journal of Physics: Conference Series **35**, 17 (2006).
[71] K. Varga and J. A. Driscoll, *Computational Nanoscience* (Cambridge University Press, 2011).
[72] A.-M. Uimonen *et al.*, Journal of Physics: Conference Series **220**, 012018 (2010).
[73] G. Stefanucci, Phys. Rev. B **75**, 195115 (2007).
[74] E. Khosravi, G. Stefanucci, S. Kurth, and E. Gross, Phys. Chem. Chem. Phys. **11**, 4535 (2009).
[75] M. E. Casida, Time-dependent density functional response theory of molecular systems: Theory, computational methods, and functionals, in *Recent Developments and Applications of Modern Density Functional Theory*, edited by J. Seminario, , Theoretical and Computational Chemistry Vol. 4, pp. 391 – 439, Elsevier, 1996.
[76] M. Strange, I. S. Kristensen, K. S. Thygesen, and K. W. Jacobsen, J. Chem. Phys. **128**, 114714 (2008).
[77] M. Di Ventra, S. T. Pantelides, and N. D. Lang, Phys. Rev. Lett. **84**, 979 (2000).
[78] N. Sergueev, L. Tsetseris, K. Varga, and S. Pantelides, Phys. Rev. B **82**, 073106 (2010).
[79] K. Varga and S. T. Pantelides, Phys. Rev. Lett. **98**, 076804 (2007).
[80] F. Evers, F. Weigend, and M. Koentopp, Phys. Rev. B **69**, 235411 (2004).
[81] H. Kondo, H. Kino, J. Nara, T. Ozaki, and T. Ohno, Phys. Rev. B **73**, 235323 (2006).
[82] E. G. Emberly and G. Kirczenow, Phys. Rev. Lett. **91**, 188301 (2003).
[83] J. Tomfohr and O. F. Sankey, The Journal of Chemical Physics **120**, 1542 (2004).
[84] S. Yeganeh, M. A. Ratner, M. Galperin, and A. Nitzan, Nano Letters **9**, 1770 (2009), http://pubs.acs.org/doi/pdf/10.1021/nl803635t.
[85] P. Delaney and J. C. Greer, Phys. Rev. Lett. **93**, 036805 (2004).
[86] M. A. Reed, C. Zhou, C. J. Muller, T. P. Burgin, and J. M. Tour, Science **278**, 252 (1997), http://www.sciencemag.org/content/278/5336/252.full.pdf.
[87] M. Tsutsui, Y. Teramae, S. Kurokawa, and A. Sakai, Applied Physics Letters **89**, 163111 (2006).
[88] Xiao, Xu, and N. J. Tao, Nano Letters **4**, 267 (2004), http://pubs.acs.org/doi/pdf/10.1021/nl035000m.
[89] J. Ulrich *et al.*, The Journal of Physical Chemistry B **110**, 2462 (2006), http://pubs.acs.org/doi/pdf/10.1021/jp056455y.
[90] S. Ghosh *et al.*, Applied Physics Letters **87**, 233509 (2005).
[91] K. Horiguchi, S. Kurokawa, and A. Sakai, The Journal of Chemical Physics **131**, 104703 (2009).
[92] X. Wu, Q. Li, J. Huang, and J. Yang, The Journal of Chemical Physics **123**, 184712 (2005).
[93] S. Ye, L. Fang, and Y. Lu, Phys. Chem. Chem. Phys. **11**, 2480 (2009).
[94] Q. Li, X. Wu, J. Huang, and J. Yang, Ultramicroscopy **105**, 293 (2005), Proceedings of the Sixth International Conference on Scanning Probe Microscopy, Sensors and Nanostructures.
[95] Y. Xue and M. A. Ratner, Phys. Rev. B **68**, 115407 (2003).
[96] R. Stadler and K. W. Jacobsen, Phys. Rev. B **74**, 161405 (2006).
[97] C. Toher, A. Filippetti, S. Sanvito, and K. Burke, Phys. Rev. Lett. **95**, 146402 (2005).
[98] C. Toher and S. Sanvito, Phys. Rev. Lett. **99**, 056801 (2007).
[99] K. S. Thygesen, Phys. Rev. Lett. **100**, 166804 (2008).
[100] S. Kümmel, L. Kronik, and J. P. Perdew, Phys. Rev. Lett. **93**, 213002 (2004).
[101] J. S. Evans, O. A. Vydrov, and T. V. Voorhis, The Journal of Chemical Physics **131**, 034106 (2009).
[102] A. Bodor and L. Diósi, Phys. Rev. A **73**, 064101 (2006).
[103] J. Yuen-Zhou, C. Rodriguez-Rosario, and A. Aspuru-Guzik, Phys. Chem. Chem. Phys. **11**, 4509 (2009).
[104] D. Neuhauser and K. Lopata, The Journal of Chemical Physics **129**, 134106 (2008).
[105] M. Di Ventra and R. D'Agosta, Phys. Rev. Lett. **98**, 226403 (2007).
[106] G. Vignale and W. Kohn, Phys. Rev. Lett. **77**, 2037 (1996).